

Photocatalytic reduction of CO₂ into CH₄ using Pd and Zn-codoped TiO₂ photocatalysts

Lanzijian, Limei Guo, Yanlong Yu and Yaan Cao*,†

(†Key Laboratory of Weak-Light Nonlinear Photonics, Ministry of Education, TEDA Applied Physics School and School of Physics, Nankai University, Tianjin 300457, China)

1. Introduction

Increasing levels of greenhouse gases in the atmosphere is the primary cause of global warming and climate change. Release of carbon dioxide (CO₂) from fossil fuel combustion is the major contributor to this phenomenon. Hence, ^[50] reduction of CO₂ into valuable hydrocarbons has been regarded as one of the most promising solutions to both the global warming and the energy shortage problems. A research focusing on the economic photocatalytic reduction of CO₂ to form products of interest was carried out using various semiconductor catalysts.^[4–6] Generally, CO₂ in the presence of water vapor can be photoreduced to methane using various semiconductor catalysts. Among the applied photocatalysts, such as TiO₂, CdS, ZrO₂ and ZnO, TiO₂ has been considered the most appropriate candidate for photocathlytic process as it is inert, relatively low cost, corrosion resistant and the most photoactive. Besides, its conduction band energy ($E_{cb} \approx -0.5$ eV (vs. NHE at pH 7)) is comparable to the reduction potentials of CO₂ (e.g., the later is -0.24 V vs. NHE for reduction of CO₂ to methane in aqueous solution at pH 7)^[6,7]. Yet, it has so far yielded only low carbon dioxide conversion rates despite using ultraviolet illumination for band gap excitation ^[6,8].

An increased CO₂ conversion efficiency was observed when the TiO₂ surface was loaded with metals, which functioned as “charge-carrier traps” and suppressed recombination of photoexcited electron-hole pairs. Tseng et al. ^[6] used sol-gel derived Cu/TiO₂ catalysts for CO₂ photoreduction in aqueous phase and found the yield of methanol is much higher than those without Cu loading. Li et al.^[13] reported both markedly increase of CO₂ photo-conversion efficiency by Cu/TiO₂ catalyst dispersed

on mesoporous silica and selective CH₄ production of due to Cu loading. Another research done by Ishitani et al. ^[9] reported that CO₂ photoreduction using Pd, Rh, Pt, Au, Cu, and Ru deposited on TiO₂ photocatalyst produces CH₄ and acetic acid, with Pd/TiO₂ exhibiting high selectivity for CH₄ production. However, too high a concentration of metal dopant may form recombination centers which could reduce photocatalytic efficiency. Though metal modifications on TiO₂ have apparent enhancement in charge separation, they have limited contribution to extending the photo-response to visible light region. Sasirekha et al. ^[18] observed that Ru doped TiO₂ has almost the same absorption spectra as the undoped TiO₂. Dholam and Patel ^[19] reported that Cr and Fe doped TiO₂ prepared by a sol–gel method had a very limited effect on inducing a red-shift in TiO₂ absorption spectra compared to those prepared by a magnetron sputtering method.

On the other hand, it has been widely reported that doping or co-doping TiO₂ with nonmetals (e.g. C, N, S, F, etc.) has resulted in more significant band gap narrowing compared to metal doping, leading to high photocatalytic efficiency under visible light irradiation ^[20–26]. Wu et al. ^[26] reported that the band gaps of N doped and N-B codoped TiO₂ were 2.16 and 2.13 eV, respectively, much smaller than that of pure TiO₂ (3.18 eV for anatase). Varghese et al. ^[8] reached high-rate solar photocatalytic conversion of CO₂ and H₂O to hydrocarbons by using N-doped TiO₂ nanotubes with Pt and/or Cu as co-catalysts.

In this work, the palladium and zinc codoped TiO₂ photocatalysts were prepared via the sol-gel technique by using Ti(OC₄H₉)₄, PdCl₂ and Zn(NO₃)₂·6H₂O as precursors. Reduction of carbon dioxide into methane in the presence of water is used to evaluate the photocatalytic activity. It is found that palladium and zinc codoped TiO₂ exhibits a higher photocatalytic performance under xenon lamp illumination than pure TiO₂, zinc-doped TiO₂ and palladium-doped TiO₂. The mechanism of the improved photocatalytic activity of Pd and Zn codoped TiO₂ under xenon lamp irradiation was discussed correspondingly.

2. Experimental Section

2.1. Materials. Deionized water (18.2 MΩ·cm) was used for all experiments. All other reagents were analytical grade and were purchased from Tianjin Letai Chemical Industry Co., Ltd. All chemicals were used without further purification.

2.2. Photocatalyst Preparation

At room temperature, an appropriate amount of Palladium chloride (PdCl₂) was dissolved in 40 mL of anhydrous ethanol. Subsequently, 1 mL of a concentrated HCl solution (12 mol/L) and 12 mL of tetrabutyl titanate (Ti(OC₄H₉)₄) were added dropwise to anhydrous ethanol under vigorous stirring. The calculated amount of Zinc nitrate hexahydrate (Zn(NO₃)₂·6H₂O) was added to the solution. Then, 1 mL of deionized water was added for further hydrolysis. After aging at room temperature for 24 h, the obtained TiO₂ sol turned into gel with constant stirring, which was dried at 100 °C for 12 h, and then triturated to powder in an agate mortar. The powder was calcined at 450 °C for 2.5 h. A set of Pd and Zn codoped TiO₂ samples were prepared by changing the amount of PdCl₂ and Zn(NO₃)₂·6H₂O added in the ethanol and designated as Pd_{X%}/Zn_{Y%}-TiO₂, where “X%” and “Y%” represented the nominal molar percentage content of Pd and Zn to Ti in TiO₂, respectively. Pd_{1.5}/Zn₅-TiO₂ was prepared by the hydrolysis of Ti(OC₄H₉)₄ in the coexistence of 91.72 mg of PdCl₂ and 519 mg of Zn(NO₃)₂·6H₂O. Palladium-doped TiO₂ (Pd-TiO₂), zinc-doped TiO₂ (Zn-TiO₂), and pure TiO₂ were prepared using the same procedure, but with the addition of the corresponding doping reagent.

2.3. Catalyst characterization

X-Ray diffraction (XRD) patterns were acquired on a Rigaku D/max 2500 X-ray diffraction spectrometer (Cu Ka, $\lambda=1.54056 \text{ \AA}$) at a scan rate of $0.02^\circ 2\theta \text{ s}^{-1}$. The average crystal size was calculated using the Scherrer equation ($D=k\lambda/B\cos\theta$). After degassing at 180 °C, the BET surface area was determined via the measurement of nitrogen adsorption–desorption isotherms at 77 K (Micromeritics Automatic Surface Area Analyzer Gemini 2360, Shimadzu). X-Ray photoelectron spectroscopy (XPS) measurements were carried out with an ESCA Lab 220i-XL spectrometer by using an unmonochromated Al Ka X-ray source (148.6 eV). All spectra were calibrated using the binding energy (BE) of the adventitious C1s peak at 284.6 eV. Diffuse reflectance

UV-vis absorption spectra (UV-Vis DRS) were collected with a UV-vis spectrometer (U-4100, Hitachi). Photoluminescence (PL) spectra were acquired by using the 325 nm line of a nano-second Nd:YAG laser (NL303G) as excitation source. The experimental setup consists of a spectrometer (Spex 1702), a photomultiplier tube (PMT, Hamamatsu R943), a lock-in amplifier, and a computer for data processing. All of the measurements were carried out at room temperature (25 ± 2 °C). The surface photovoltage spectroscopy (SPS) was measured on a solid-junction photovoltaic cell of indium tin oxide (ITO)/sample/ITO equipped with a lock-in amplifier (Model SR830, DSP) and synchronized with a light chopper. The monochromatic light was obtained by passing light from a 500W xenon lamp (CHF-XQ 500W) through a double prism monochromator (WDG30-2).

2.4. Evaluation of Photocatalytic Activity

In the photocatalytic reduction of CO₂, 150 mg photocatalyst was uniformly dispersed on the nanoparticulate film with an area of 9.4 cm² which was placed at the bottom of a sealed Pyrex glass reaction vessel (410 mL). 2 mL of deionized water was injected into the reaction system as reducer. A 500 W Xenon arc lamp was used as the light source of photocatalytic reaction. Prior to the illumination, the high purity of CO₂ gas (99.99%), via a flow controller, was followed into the reaction setup for 45 min for reaching ambient pressure. During irradiation, about 0.4 mL of gas was continually taken from the reaction cell every 2 h for subsequent CH₄ and CO concentration analysis by using a gas chromatograph (Techcomp GC-7890F, equipped with a 1 m× ϕ 3 mm TDX-01 packed column and a flame ionization detector (FID)). N₂ was used as the carrier gas. Since FID cannot detect CO and CO₂, an additional converter (Techcomp converter loaded with Ni catalyst) was attached to the GC system between the column and detector, which can reduce CO to methanol ($\text{CO} + \text{H}_2 \rightarrow \text{CH}_3\text{OH}$) and CO₂ to methane ($\text{CO}_2 + 4\text{H}_2 \rightarrow \text{CH}_4 + 2\text{H}_2\text{O}$). Hence, CO and CO₂ could be analyzed simultaneously.

3. Results and Discussion

Photocatalytic activity

Photoreduction of CO₂ into hydrocarbon fuel (CH₄) in the presence of water under irradiation of Xxeon arc lamp is used to evaluate the photocatalytic activity of the samples. Gas chromatographic analysis shows that CH₄ was exclusively obtained as the reduction product and CO as intermediate product. Fig. 1 shows the photogenerated CH₄ (a) and CO (b) from CO₂ over different photocatalysts. The photocatalytic results are summarized in Table 1. In the case of pure TiO₂ as photocatalyst, CO (8.99×10^{-6} mol) was observed as a major product, with a small amount of CH₄ (3.50×10^{-7} mol). In the case of Pd and/or Zn doped TiO₂, a considerable amount of CH₄ was formed, however, the amount of CO produced was reduced compared with the obtained using TiO₂. The pure TiO₂ photocatalyst shows trifling photocatalytic activity toward CH₄ production, which exhibits comparable activity to that of TiO₂(P25), while Zn₅-TiO₂ and Pd_{1.5}-TiO₂ exhibit an obvious improvement in the photocatalytic activity. Pd_{1.5}/Zn₅-TiO₂ shows the highest activity among all the samples, for which the total yield of CH₄ obtained in the experiment after 8 h of continuous irradiation was 7.99×10^{-6} mol. Its specific photocatalytic activity was about 23.3, 9 and 2.2 times that of pure TiO₂, Pd_{1.5}-TiO₂ and Zn₅-TiO₂, indicating that co-doping TiO₂ with palladium and zinc is an effective way for preparing TiO₂-based catalysts with a high photoactivity. The photocatalyst of Degussa P25 was measured under the same condition.

The ratio between the CO and CH₄ produced was strongly dependent on the amount of deposited Pd and Zn on TiO₂ (Figure 3(a)-(b)). As shown in fig.2, an increase of the amount of Pd from 0 to 3 wt% caused both an increase in the CH₄ and a decrease in the CO formation.^{[3] [77]} The amount of CH₄ reaches a maximum at 3 wt%, follows by a sharp decrease with further loading of Pd.

Figure 3 shows the effect of Zn content on the yield of photocatalytic product using prepared Pd_{1.5}/Zn_x-TiO₂ samples. It can be seen that the amount of CH₄ is dependent on the content of Zn. In batch reaction, the products yield increased with the increase of Zn content, accompanied by a decrease in the CO yields, then decreased as Zn content exceeded 5%. On the basis of these results, we chose Pd_{1.5}/Zn₅-TiO₂ as the photocatalyst for the following experiments.

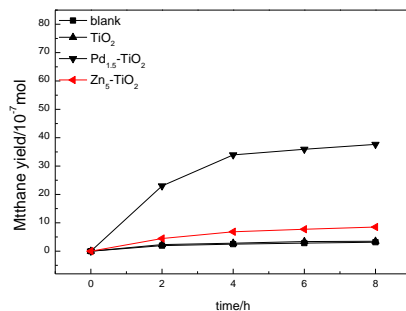


Fig.1 Photocatalytic CH₄(a) and CO(b) formation by pure TiO₂, Pd_{1.5}-TiO₂, Zn₅-TiO₂ and Pd_{1.5}/Zn₅-TiO₂ samples

Table 1 Photocatalytic activity of pure TiO₂, Zn₅-TiO₂, Pd_{1.5}-TiO₂ and Pd_{1.5}/Zn₅-TiO₂ samples under Xenon arc lamp irradiation

Sample	CH ₄ generation amount (mol)	specific	CO generation amount (mol)	specific
		photocatalytic activity ^b		photocatalytic activity ^c
		(mol·g ⁻¹ ·h ⁻¹)		(mol·g ⁻¹ ·h ⁻¹)
blank ^a	3.14×10 ⁻⁷	-	2.34×10 ⁻⁶	-
TiO ₂ (P25)	3.58×10 ⁻⁷	2.98×10 ⁻⁷	1.02×10 ⁻⁵	8.5×10 ⁻⁶
TiO ₂	3.50×10 ⁻⁷	2.91×10 ⁻⁷	8.99×10 ⁻⁶	7.49×10 ⁻⁶
Zn ₅ -TiO ₂	8.51×10 ⁻⁷	7.09×10 ⁻⁷	8.53×10 ⁻⁶	7.11×10 ⁻⁶
Pd _{1.5} -TiO ₂	3.59×10 ⁻⁶	2.99×10 ⁻⁶	4.27×10 ⁻⁷	3.56×10 ⁻⁷
Pd _{1.5} /Zn ₅ -TiO ₂	7.99×10 ⁻⁶	6.66×10 ⁻⁶	3.88×10 ⁻⁶	3.23×10 ⁻⁶
Pd _{1.5} /Zn ₃ -TiO ₂	6.48×10 ⁻⁶	5.40×10 ⁻⁶	6.22×10 ⁻⁶	5.18×10 ⁻⁶
Pd _{1.5} /Zn ₇ -TiO ₂	3.77×10 ⁻⁶	3.14×10 ⁻⁶	7.42×10 ⁻⁶	6.18×10 ⁻⁶
Pd _{2.5} /Zn ₅ -TiO ₂	8.08×10 ⁻⁶	6.73×10 ⁻⁶	6.84×10 ⁻⁷	5.70×10 ⁻⁷
Pd ₃ /Zn ₅ -TiO ₂	8.31×10 ⁻⁶	6.93×10 ⁻⁶	5.75×10 ⁻⁷	4.79×10 ⁻⁷
Pd ₅ /Zn ₅ -TiO ₂	7.14×10 ⁻⁶	5.95×10 ⁻⁶	1.75×10 ⁻⁷	1.46×10 ⁻⁷
Pd ₇ /Zn ₅ -TiO ₂	5.44×10 ⁻⁶	4.53×10 ⁻⁶	3.47×10 ⁻⁷	2.89×10 ⁻⁷

^aBlank is the photolysis of CO₂; ^bspecific photocatalytic activity of CH₄, CH₄ generation amount per unit mass catalyst per hour;

3.1 XRD patterns

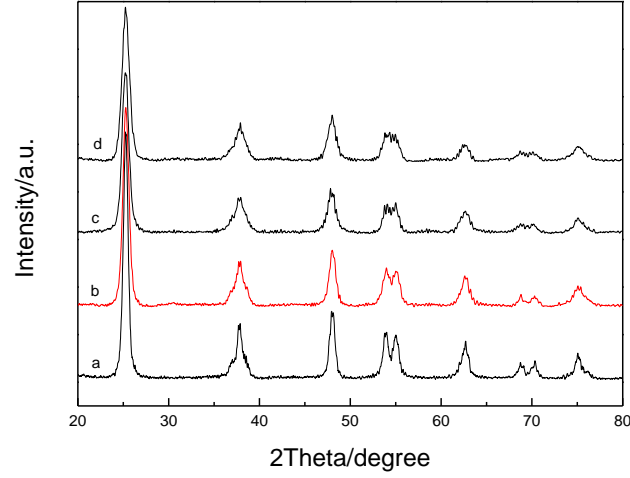


Fig. 4 XRD patterns of pure TiO₂(curve a), Pd_{1.5}-TiO₂ (curve b), Zn₅-TiO₂ (curve c) and Pd_{1.5}/Zn₅-TiO₂ (curve d) samples

Inset is the enlarged XRD peaks of crystal plane (101)

Samples	Lattice parameter (Å)			cell	crystal	S _{BET} (m ² g ⁻¹)
	a	b	c	volume (Å ³)	size (nm)	
TiO ₂	3.7857	3.7857	9.5118	136.32	12.4	56.9353
Pd _{1.5} -TiO ₂	3.7842	3.7842	9.5042	136.10	9.6	74.6179
Zn ₅ -TiO ₂	3.7876	3.7876	9.4963	136.23	8.9	63.4306
Pd _{1.5} /Zn ₅ -TiO ₂	3.7851	3.7851	9.4875	135.93	7.7	79.2025

Table 2 The cell parameters, crystallite sizes and specific surface areas of pure

TiO₂, Zn₅-TiO₂, Pd_{1.5}-TiO₂ and Pd_{1.5}/Zn₅-TiO₂ sample

Fig.4 shows the XRD patterns of pure TiO₂(curve a), Pd_{1.5}-TiO₂ (curve b), Zn₅-TiO₂ (curve c) and Pd_{1.5}/Zn₅-TiO₂ (curve d) samples in the range of 10-80°(2θ). It is found that the majority of the crystal phase is anatase for all of the samples. The shape of Zn₅-TiO₂ and Pd_{1.5}/Zn₅-TiO₂ is consistent with that of pure TiO₂. Doping Zn does not produce any new diffraction peaks. For Pd_{1.5}-TiO₂ (curve b), besides the anatase peaks, diffraction peak at 29.9° (29.3 jade) can also be observed, corresponding to the crystal plane of (100) of PdO. This indicates that a small amount of PdO was formed in the Pd_{1.5}-TiO₂ during the doping process. However, the diffraction peak of PdO is not

observed in the Pd_{1.5}/Zn₅-TiO₂ sample, suggesting that the addition of Zn can inhibited the formation of PdO. The diffraction peak of crystal planes (101) was selected to estimate the crystal size of all samples by the Debye-Scherrer equation.⁷¹ The results indicated that the crystallite size of the pure TiO₂ is 12.4 nm, while the doped particles have much smaller size (less than 10 nm). As a result, the doped TiO₂ has significantly higher specific surface area, as shown in Table 2.

It is documented that there are two kinds of doping modes, interstitial and substitutional, for doped metal ions in oxides.⁸¹ In the case of the interstitial mode, the ionic radius of dopant should be smaller than that of the lattice metal ion and the oxide lattice spacing, allowing the doping metal ions to enter into the crystal cell of the oxide. The ionic radius of the doping Zn²⁺ ion (74 pm) is larger than that of the lattice Ti⁴⁺ ion (53 pm); it is impossible for the Zn²⁺ ions to enter into the crystal cell of TiO₂ through the interstitial mode. Upon doping through the substitutional mode, the doping metal ions will substitute the lattice metal ions and thus occupy the positions of the lattice metal ions in the oxide. If the Zn²⁺ ions to replace and occupy lattice Ti⁴⁺ ion ions, the lattice parameters and cell volume of the doped TiO₂ should be larger than that of pure TiO₂. As a result, the positions of all of the diffraction peaks in XRD patterns should shift to lower diffraction angles. It is seen that no shift of the peaks was observable in the XRD patterns of the zinc doped TiO₂, as shown in Figure 4, and the lattice parameters and cell volume of Zn₅-TiO₂ and Pd_{1.5}/Zn₅-TiO₂ were almost the same as those of pure TiO₂, as shown in Table 2. Thus, it is reasonable to suppose that the Zn²⁺ ions are doped on the surface of TiO₂. As shown in Fig. 4, doping palladium in Pd_{1.5}-TiO₂ and Pd_{1.5}/Zn₅-TiO₂ does not cause any shift in diffraction angles, indicating that Pd ions do not enter the TiO₂ lattice and exist as small crystallites on the particle surface, similar to the case of doping Zn.

3.2 XPS analysis

XPS measurements were carried out to investigate the chemical states of all of the elements in the pure TiO₂, Pd_{1.5}-TiO₂, Zn₅-TiO₂ and Pd_{1.5}/Zn₅-TiO₂ samples. The peak positions of all of the elements in TiO₂ and doped TiO₂ samples are illustrated in Table 2. ^[60]For the pure TiO₂, the peak of Cl2p_{3/2} at 198.2 eV is the same as that of

Cl2p_{3/2} in TiCl₄ (198.2 eV),³³ which is assigned to the Cl⁻ ions linked with Ti⁴⁺. Since the ionic radius of Cl⁻ ion is larger than that of O²⁻ (1.81 Å versus 1.40 Å), lattice O²⁻ in TiO₂ cannot be substituted by Cl⁻ during the reactions.³⁴ Thus, it is deduced that the Cl⁻ ions should be located on the TiO₂ surface via the coordination with the unsaturated Ti⁴⁺ sites.

Figure 7 shows the Zn2p XPS spectra of Zn₅-TiO₂ and Pd_{1.5}/Zn₅-TiO₂ samples. The peak at 1022.0-1022.1 eV is assigned to Zn2p_{3/2}, respectively, which are located between in metallic Zn (1021.8 eV) and ZnO (1022.5 eV). It is indicated that the doping Zn²⁺ ions that substitute lattice Ti in Zn₅-TiO₂ and Pd_{1.5}/Zn₅-TiO₂ samples.

In the Cl2p XPS spectra of Zn₅-TiO₂ and Pd_{1.5}/Zn₅-TiO₂ samples (see Figure 8), the binding energies of Cl2p_{3/2} are identified to be 198.7-199.0 eV, which are located between those of Cl2p_{3/2} in TiCl₄ (198.2 eV)³³ and Cl 2p_{3/2} in ZnCl₂ (199.7 eV). These results suggest that the Zn²⁺ ions link with the unsaturated oxygen and Cl⁻ ions, respectively, thus meaning the formation of O-Zn-Cl structure on the surface of Zn₅-TiO₂ and Pd_{1.5}/Zn₅-TiO₂ samples. A part of the Cl⁻ ions may also link with the unsaturated Ti to form the O-Ti-Cl structure.

Pure TiO₂ shows Ti2p peaks assigned to Ti2p_{3/2} and Ti2p_{1/2} at 458.7 and 464.4 eV (Figure 5) and an O1s peak assigned to lattice O²⁻ at 529.9 eV (Figure 6). In the case of Zn₅-TiO₂ and Pd_{1.5}/Zn₅-TiO₂ samples, all of the peaks of Ti2p and O1s of TiO₂ present higher binding energies after the doping of Zn²⁺, which is consistent with the formation of O-Zn-Cl structure on the TiO₂ surface after the doping. The Pauling electronegativity of Zn²⁺ ion (1.7) in the Ti-O-Zn-Cl structure is larger than that of the Ti⁴⁺ ion (1.5) in the Ti-O-Ti structure, which will induce the possible electron transfer from Ti⁴⁺ and O²⁻ to Zn²⁺ in the Ti-O-Zn-Cl structure. Such a charge transfer will make Ti⁴⁺ and O²⁻ be poorer in electrons and thus result in an increase in the binding energies of Ti2p and O1s core electrons. It is noted that, in Table 3, the O1s signals present shoulders located at the side of higher binding energy, which are assigned to the OH species on the surface. It is clear that the amount of the hydroxyl groups on the TiO₂ surface increased greatly after being doped by Zinc.

^[10]Further information of the surface can be also obtained from the Pd3d XPS

spectrum. The Pd3d peaks of Pd_{1.5}-TiO₂ and Pd_{1.5}/Zn₅-TiO₂ samples are presented in Fig. 7. The peaks at 342.1 eV and 336.8 eV are assigned to Pd²⁺. This result indicated that dopant Pd existed as PdO in TiO₂.^[19,20]

Fig. 8^[35] shows the O1s XPS spectra of pure and doped TiO₂. The broad and asymmetric peaks indicate that there are at least two types of oxygen species on the surface according to the binding energy range from about 528 to 533 eV. Fitting of the curves gives two components centered at 530.1 and 531.9 eV, which are assigned to lattice oxygen (O-Ti) and surface-bound hydroxyl groups (OHs), respectively^[40]. Their relative content is also summarized in Table 3. It can be see that, doping Zn significantly increase the content of surface-bound OHs. Specifically, Pd_{1.5}/Zn₅-TiO₂ exhibits the highest content of surface-bound OHs.

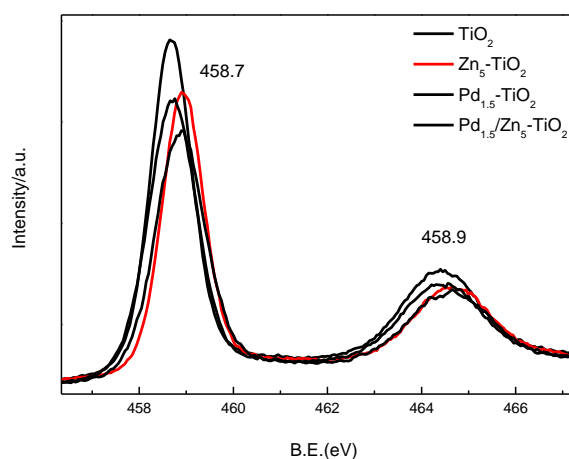


Fig.5 XPS spectra of Ti2p on pure TiO₂, Zn₅-TiO₂, Pd_{1.5}-TiO₂ and Pd_{1.5}/Zn₅-TiO₂ samples

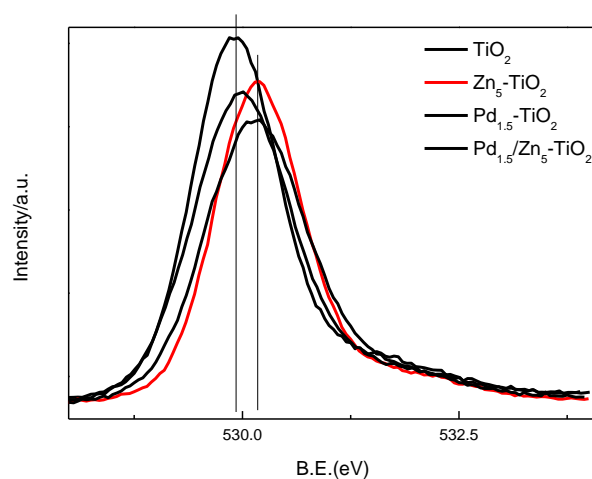


Fig.6 XPS spectra of O1s on pure TiO_2 , $\text{Zn}_5\text{-TiO}_2$, $\text{Pd}_{1.5}\text{-TiO}_2$ and $\text{Pd}_{1.5}/\text{Zn}_5\text{-TiO}_2$ samples

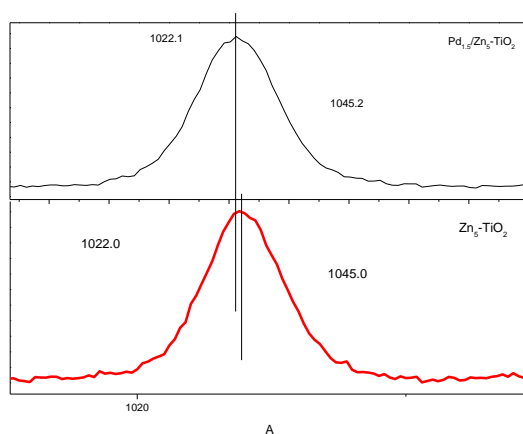


Fig.7 XPS spectra of Zn2p on $\text{Zn}_5\text{-TiO}_2$ and $\text{Pd}_{1.5}/\text{Zn}_5\text{-TiO}_2$ samples

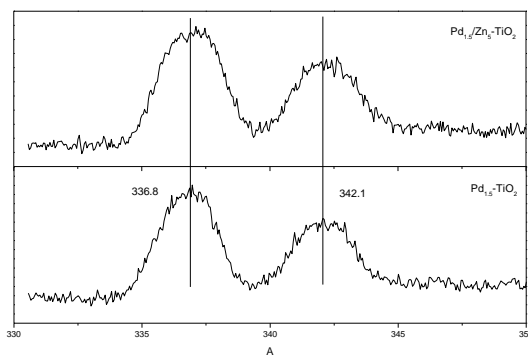


Fig.8 XPS spectra of Pd3d on Pd_{1.5}-TiO₂ and Pd_{1.5}/Zn₅-TiO₂ samples**Table 2:** Peak Positions (eV) and Assignments of the pure TiO₂, Pd_{1.5}-TiO₂, Zn₅-TiO₂ and Pd_{1.5}/Zn₅-TiO₂ samples

Samples	O1s		Ti2p		Cl2p		Zn2p		Pd3d	
	O _H	O _L	Ti2p _{3/2}	Ti2p _{1/2}	Cl2p _{3/2}	Cl2p _{1/2}	Zn2p _{3/2}	Zn2p _{1/2}	Pd3d _{7/2}	Pd3d _{5/2}
	1s(O-H)	1s(Ti-O)								
TiO ₂	531.9	530.0	458.7	464.4	198.2	199.6				
Pd _{1.5} -TiO ₂	531.9	530.1	458.7	464.4	198.2	199.8			336.8	342.1
Zn ₅ -TiO ₂	531.9	530.1	458.9	464.6	199.0	200.6	1022.1	1045.2		
Pd _{1.5} /Zn ₅ -TiO ₂	531.9	530.1	458.9	464.6	198.7	200.1	1022.0	1045.0	336.8	342.1

Table 3 Surface properties of pure TiO₂, Zn₅-TiO₂, Pd_{1.5}-TiO₂ and Pd_{1.5}/Zn₅-TiO₂ samples derived from XPS characterization

Samples		O _L (O-Ti)	O _H (O-H)	Atomic surface concentration				
				Ti	Zn	Pd	Zn/Ti	Pd/Ti
TiO ₂	E _b /eV	530.1	531.9	19.96				
	fwhm	1.03	1.0					
	r _i /%	91.3	8.7					
Pd _{1.5} -TiO ₂	E _b /eV	530.0	531.9	20.28		0.76		0.04
	fwhm	1.15	1.86					
	r _i /%	92.0	8.0					
Zn ₅ -TiO ₂	E _b /eV	530.1	531.9	18.26	7.22		0.39	
	fwhm	1.03	1.96					
	r _i /%	89.9	10.1					
Pd _{1.5} /Zn ₅ -TiO ₂	E _b /eV	530.1	531.9	20.37	4.35	0.61	0.21	0.03
	fwhm	1.21	2.31					
	r _i /%	89.5	10.5					

3.3 Raman spectra

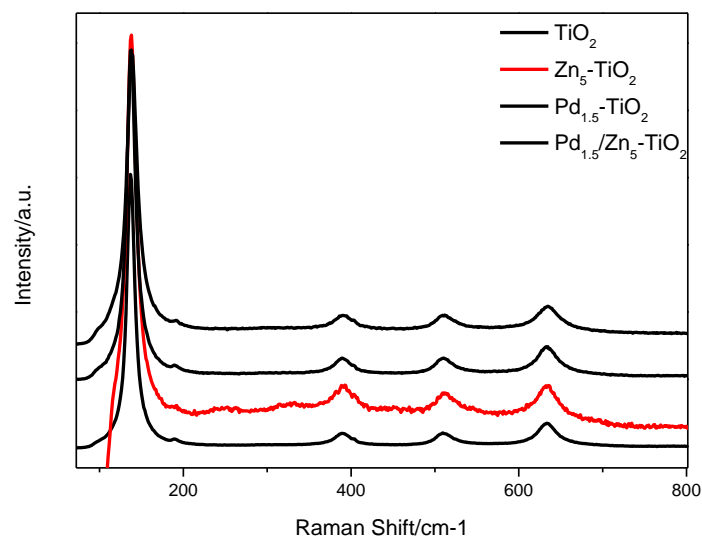


Fig.10 Raman spectra of the pure TiO_2 , $\text{Zn}_5\text{-TiO}_2$, $\text{Pd}_{1.5}\text{-TiO}_2$ and $\text{Pd}_{1.5}/\text{Zn}_5\text{-TiO}_2$ samples

Raman spectra were recorded to further investigate the formation of the surface species (Figure 10). All of the samples show characteristic bands at 138, 190, 390, 512, and 634 cm^{-1} , which are assigned to the E_g , B_{1g} , A_{1g} , B_{2g} , and E_g vibrational modes of TiO_2 , respectively, indicating the presence of the anatase phase in all of these samples.²⁹ Except these peaks, some additional peaks around 256 and 333 cm^{-1} were observed for the $\text{Zn}_5\text{-TiO}_2$. Rubim et al. have reported that the feature at 326 cm^{-1} was tentatively assigned to the antisymmetric Zn-Cl stretching belonging to the T_2 species in a T_d symmetry. Quicksall and Spiro have assigned the feature at 265 cm^{-1} to the A_1 and T_2 Zn-Cl stretching modes. Therefore, we ascribed these peaks to the vibrational mode of Zn-Cl bonds. Furthermore, in comparison to the Raman peak at 437 cm^{-1} , which was attributed to the E_2 mode of ZnO, the peaks around 450 cm^{-1} was supposed to be related to the Zn-O. The Raman spectra suggested the existence of both Zn-O and Zn-Cl bonds as the surface chemical species of the Zn doped TiO_2 , which is consistent with the results of XPS that O-Zn-Cl was formed on the surface of $\text{Zn}_5\text{-TiO}_2$.

3.4 UV-Vis DRS

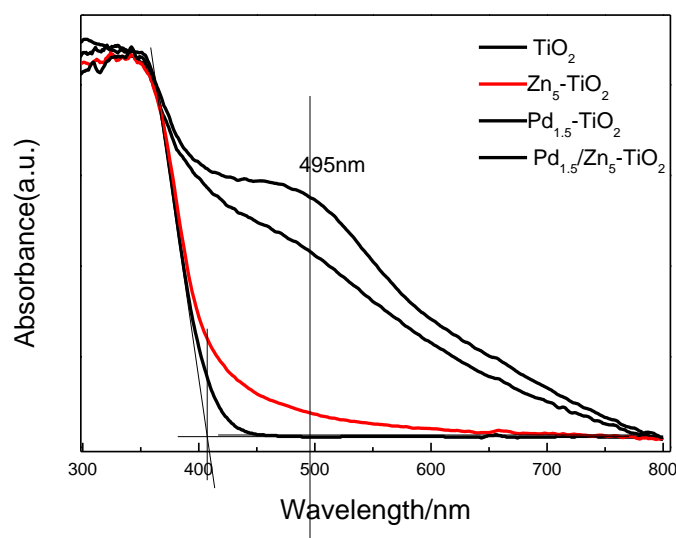


Fig.11 Diffuse reflectance UV-Vis spectra of pure TiO_2 , $\text{Zn}_5\text{-TiO}_2$, $\text{Pd}_{1.5}\text{-TiO}_2$ and $\text{Pd}_{1.5}/\text{Zn}_5\text{-TiO}_2$ samples

Fig. 11 shows the UV-vis absorption spectra of the pure TiO_2 , $\text{Pd}_{1.5}\text{-TiO}_2$, $\text{Zn}_5\text{-TiO}_2$ and $\text{Pd}_{1.5}/\text{Zn}_5\text{-TiO}_2$ samples. The pure TiO_2 shows a strong peak at 350 nm, which is mainly attributed to the electron transitions from the valence band to conduction band (band-to-band transition, $\text{O}_{2p} \rightarrow \text{Ti}_{3d}$).^[1] The band threshold at 406 nm corresponds to a band gap of 3.05 eV. For $\text{Zn}_5\text{-TiO}_2$, $\text{Pd}_{1.5}\text{-TiO}_2$ and $\text{Pd}_{1.5}/\text{Zn}_5\text{-TiO}_2$ samples, absorption peaks at 350 nm almost no shift compared with pure TiO_2 . Compared with the pure TiO_2 , Zn-TiO_2 shows a distinct hump at 430 nm, which is contributed to the doping energy level of Zn^{2+} ions located at 0.17 eV below the conduction band. It is suggested that the visible-light absorption of $\text{Zn}_5\text{-TiO}_2$ arises from the electronic transition from valance band to this doping energy level.^[10] As shown in Fig. 11, a broad band between 420 and 650 nm centered at 470 nm could be observed in the absorption spectra of $\text{Pd}_{1.5}/\text{TiO}_2$ owing to a d-d transition of PdO particles^[31]. The $\text{Pd}_{1.5}/\text{Zn}_5\text{-TiO}_2$ sample shows a strong absorption in the visible range from 400 to 600 nm (Fig. 5), which is stronger than $\text{Pd}_{1.5}\text{-TiO}_2$ and $\text{Zn}_5\text{-TiO}_2$ because the contribution is from both PdO and the doping energy level. This means that palladium and zinc co-doped TiO_2 catalysts are more sensitive to the visible light than pure TiO_2 , $\text{Pd}_{1.5}\text{-TiO}_2$ and $\text{Zn}_5\text{-TiO}_2$ samples.

3.4 Photoluminescence spectra

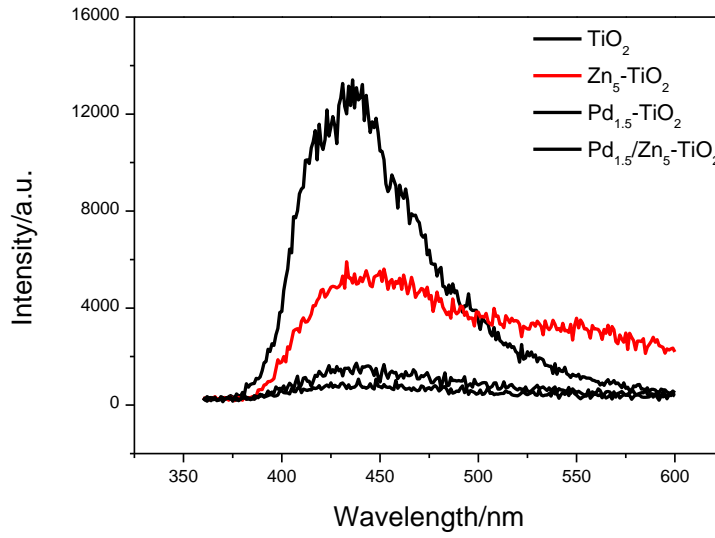


Fig. 11 Photoluminescence emission spectra of pure TiO_2 , $\text{Zn}_5\text{-TiO}_2$, $\text{Pd}_{1.5}\text{-TiO}_2$ and $\text{Pd}_{1.5}/\text{Zn}_5\text{-TiO}_2$ samples

The mechanism mentioned above can be further confirmed by photoluminescence (PL) results. After electrons are excited from valence band to conduction band upon irradiation, they can transfer to the energy levels of oxygen vacancies via a nonradiative transition, then fall into the valence band and recombine with holes, accompanied by PL emission. Hence, a decrease in the PL intensity indicates a decrease in the recombination rate and, thus, an enhanced charge separation efficiency of photoinduced electrons and holes. Fig. 11 gives the PL emission spectra of pure TiO_2 , $\text{Zn}_5\text{-TiO}_2$, $\text{Pd}_{1.5}\text{-TiO}_2$ and $\text{Pd}_{1.5}/\text{Zn}_5\text{-TiO}_2$ samples. Two peaks around 437 and 480 nm are observed for the pure TiO_2 , which is attributed respectively to the transition from oxygen vacancies with two-trapped electrons and one-trapped electron to the valence band of TiO_2 . The energy levels related to the two kinds of the oxygen vacancies are located at 0.21 and 0.47 eV below the conduction band of TiO_2 , respectively.

Compared with pure TiO_2 , it can be seen that the emission intensity of TiO_2 is weakened significantly for doped TiO_2 samples, indicating that the recombination of photogenerated carriers via transition from the oxygen vacancies to the valence band of TiO_2 is suppressed effectively upon the Zn or Pd doping, especially for the $\text{Pd}_{1.5}/\text{Zn}_5\text{-TiO}_2$ sample. For $\text{Zn}_5\text{-TiO}_2$, the emission is weaker than pure TiO_2 ,

indicating that the recombination of photogenerated carriers via transition from the oxygen vacancies to the valence band of TiO_2 is inhibited upon the Zn^{2+} ions. This observation further suggested that the surface state energy level attributed to the O-Zn-Cl species should locate between the conduction band of $\text{Zn}_5\text{-TiO}_2$ and the energy level of oxygen vacancies. Since the surface state energy level of O-Zn-Cl species which located at 0.17 eV below the conduction band in $\text{Zn}_5\text{-TiO}_2$ was higher than those of oxygen vacancies (0.21 and 0.47 eV below the conduction band), the photogenerated electrons from the conduction band prefer to move from the conduction band of TiO_2 to the surface state energy level rather than to the oxygen vacancies. As a result, the photogenerated electrons and holes tend to accumulate on the surface state energy level of TiO_2 and at the valence band of TiO_2 , respectively. Thus, the emission intensity of TiO_2 originated from the transition from the oxygen vacancies to the valence band of TiO_2 decreased greatly after being doped by Zn^{2+} ions. The PL intensity of $\text{Pd}_{1.5}\text{-TiO}_2$ was greatly decreased. It is known that the intensity of the emission from the TiO_2 particles is strongly dependent on the surface treatment of the TiO_2 particles [33]. PdO particles deposited on the surface could act as trapping sites to capture photogenerated electrons from TiO_2 conduction band, separating the photogenerated electron-hole pairs. Therefore, the recombination rate of photogenerated electrons and holes was retarded, leading to the reduction of PL signal decrease. For $\text{Pd}_{1.5}/\text{Zn}_5\text{-TiO}_2$ sample, the separation of photogenerated holes and electrons is enhanced due to the contribution from both the doping of Zn^{2+} ions and PdO, resulting in a much stronger suppressed recombination of photogenerated carriers and, thus, the lowest luminescence intensity for $\text{Pd}_{1.5}/\text{Zn}_5\text{-TiO}_2$ among all of the samples.

3.6 SPS spectra

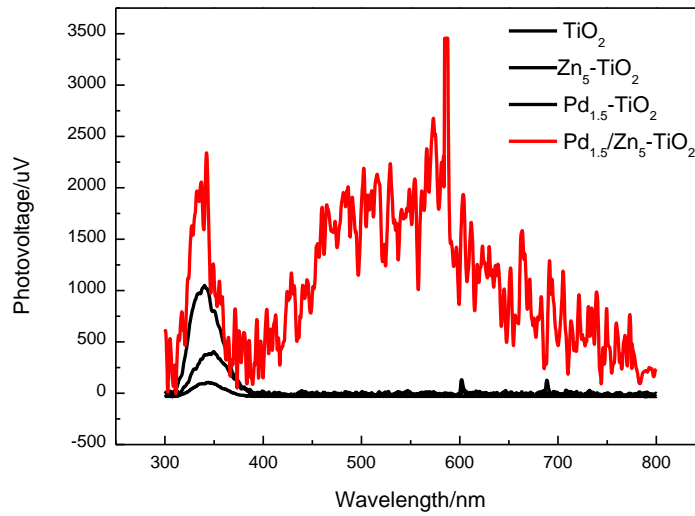


Fig. 13 SPS spectra of the pure TiO_2 , $\text{Zn}_5\text{-TiO}_2$, $\text{Pd}_{1.5}\text{-TiO}_2$ and $\text{Pd}_{1.5}/\text{Zn}_5\text{-TiO}_2$ samples

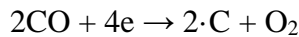
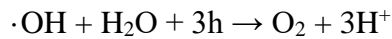
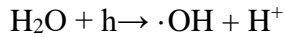
[8]The SPS is a kind of action spectrum on the basis of optical absorption. It can reflect photogenerated charge separation and transfer behavior as well as optical absorption characteristics of semiconductor samples. Fig. 11 shows the SPS spectra of the pure TiO_2 , $\text{Pd}_{1.5}\text{-TiO}_2$, $\text{Zn}_5\text{-TiO}_2$ and $\text{Pd}_{1.5}/\text{Zn}_5\text{-TiO}_2$ samples. The obvious SPS response (SPS P1), is ascribed to the band-to-band transitions ($\text{O}2p \rightarrow \text{Ti}3d$) (344 nm for TiO_2 , 340 nm for $\text{Pd}_{1.5}\text{-TiO}_2$, 349 nm for $\text{Zn}_5\text{-TiO}_2$, and 337 nm for $\text{Pd}_{1.5}/\text{Zn}_5\text{-TiO}_2$, respectively). With use of the onset edge of the spectrum (377 and 383 nm) for TiO_2 and $\text{Zn}_5\text{-TiO}_2$, the bandgap of TiO_2 and $\text{Zn}_5\text{-TiO}_2$ is determined to be 3.29 and 3.24 eV, respectively. Compare to the pure TiO_2 , the SPS response became stronger for the doped TiO_2 samples, implying that the photoinduced electron-hole pairs are easily separated on the basis of the SPS principle upon the Pd and/or Zn doping, especially for the sample codoped by Pd and Zn.^[23] Interestingly, except for an SPS P1 response, a new SPS response, with an SPS peak (P2), can be seen at the wavelength range from 390 and 800nm centered at 530 nm could be observed in the absorption spectra of $\text{Pd}_{1.5}/\text{Zn}_5\text{-TiO}_2$ owing to a $d\text{-}d$ transition of PdO particles^[31].

(For $\text{Zn}_5\text{-TiO}_2$ sample, the SPS response assigned to ZnO cannot be distinguished in that TiO_2 and ZnO have similar band structures and energy band gaps. If the sub-bands related to the SOVs are near the bottom of the conduction band, an

SPS response cannot appear near the band edge. On the contrary, a corresponding SPS response should appear if the sub-bands are located near the top of the valence band. Therefore, it can be confirmed that the sub-bands related to the SOVs are near the bottom of the conduction band. This is in accordance with the literature in theoretical calculation.^[41]) be different from UV-Vis, should choose a better one to induce the bandgap of all samples.

Discussion

The mechanism to account for photo-reduction of CO₂ involves the initial photoexcitation of the catalyst, creating photo-generated electrons (e⁻) and holes (h⁺) on the surface of the TiO₂ catalysts.^[27–29] The holes first react with water vapour adsorbed on the catalyst, resulting in producing hydroxyl radicals (·OH) and hydrogen ions (H⁺). The obtained (·OH) can react with photogenerated holes and H₂O to form H⁺ and oxygen (eqn (2)). At the same time, electrons are directly captured by the adsorbed CO₂ molecules to form CO active species during the photocatalytic process (eqn (3)). The resultant CO can react with the electrons to form carbon radicals (·C), which can further react with H⁺ generated from H₂O and e⁻ on the catalyst surface to finally produce CH₄ (eqn (4)). The presence of CO in the gaseous product mixture presumably resulted from the incomplete reduction of CO₂. It could be due to insufficient H⁺ produced from H₂O present in the reactant mixture and resulted from recombination of ·C radicals and oxygen on the surface of the catalysts.



The edge of the valence band (E_{VB}) of TiO₂ determined to be 2.18 V (vs normal

hydrogen electrode, NHE), more positive than that of $E^{\circ}(\text{H}_2\text{O}/\text{H}^+)$ ($\text{H}_2\text{O} \rightarrow \frac{1}{2}\text{O}_2 + 2\text{H}^+ + 2\text{e}^-$, $E^{\circ}_{\text{redox}} = 0.82 \text{ V}$ vs NHE), and the edge of the conduction band was estimated to be -0.87 V (vs NHE), more negative than that of $E^{\circ}(\text{CO}_2/\text{CH}_4)$ ($\text{CO}_2 + 8\text{e}^- + 8\text{H}^+ \rightarrow \text{CH}_4 + 2\text{H}_2\text{O}$, $E^{\circ}_{\text{redox}} = -0.24 \text{ V}$ (vs NHE)). This indicates that the photogenerated electrons and holes on the irradiated TiO_2 can react with adsorbed CO_2 and H_2O to produce CH_4 .

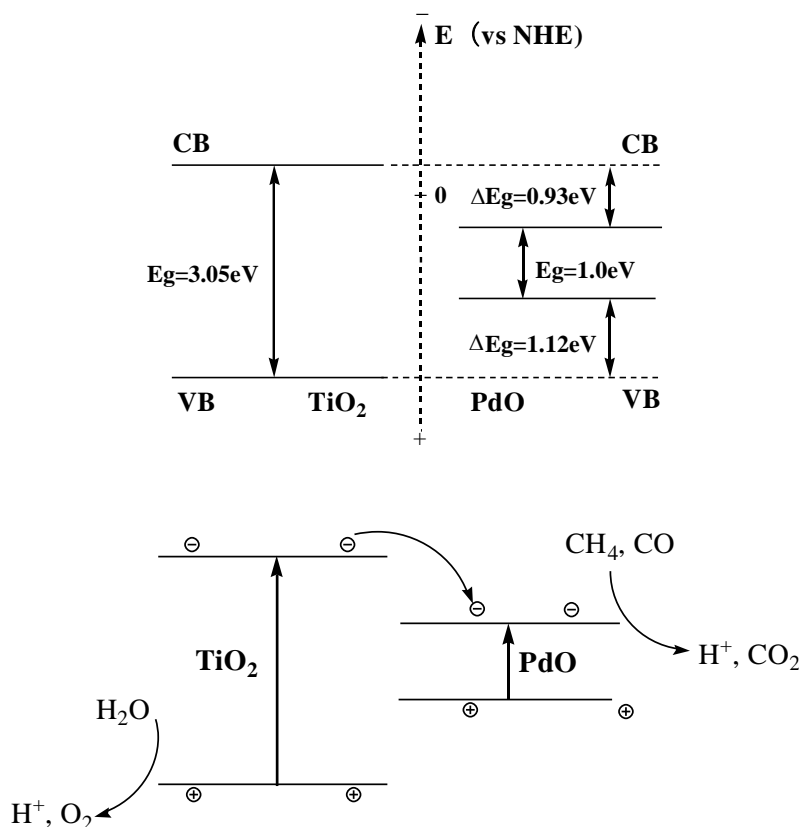


Figure 17. Scheme of photocatalytic mechanism of $\text{Pd}_{1.5}\text{-TiO}_2$ sample

The doping of Zinc ions resulted in the formation of the surface state energy level originated from the O-Zn-Cl species on $\text{Zn}_5\text{-TiO}_2$, and the appearance of the broad absorption at 400-600 nm attributed to the electronic transition from the valence band of TiO_2 to the surface state energy level. As a result, photogenerated electrons and holes can be directly and efficiently separated on the surface of TiO_2 under light irradiation illumination. The photogenerated electrons tend to accumulate at the surface state energy level, and the photogenerated holes are collected at the valence band of TiO_2 on the surface. During the photocatalytic reaction, H_2O molecules adsorbed in the surface active sites on $\text{Zn}_5\text{-TiO}_2$ are immediately oxidized by

photogenerated holes from the valence band of the catalyst to generate active species ($\cdot\text{OH}$) to produce CH_4 . Meanwhile, the photogenerated electrons accumulated at the surface state energy level, which is higher than the electrode potential CO_2/CO (NHE 0.12 eV) can be captured directly by the efficiently adsorbed CO_2 molecules on the surface of $\text{Zn}_5\text{-TiO}_2$ to form CO for further generation of carbon radicals ($\cdot\text{C}$), which can further react with photogenerated electrons and H^+ to produce CH_4 . The recombination of photogenerated carriers originated from the transition from the oxygen vacancies to the valence band of TiO_2 also decreased greatly, since the surface state energy level of O-Zn-Cl species located at 0.17 eV below the conduction band in $\text{Zn}_5\text{-TiO}_2$ was higher than those of oxygen vacancies (0.21 and 0.47 eV below the conduction band).

Fig. 17 depicts the valence and conduction bands for TiO_2 and PdO with their band gap energy. In general, the difference between conduction bands of two semiconductors is the driving forces of electron injection. Therefore, for $\text{Pd}_{1.5}\text{-TiO}_2$, under xenon lamp irradiation, the excited electrons generate in the conduction band of TiO_2 and are quickly transferred to a PdO particle since the conduction band of TiO_2 is more negative than that of PdO as shown in Fig. 7. The PdO is coupled by interparticle electron transfer from irradiated TiO_2 to its conduction band. The electrons are then scavenged by molecular oxygen CO_2 to yield CO . The new formed intermediates tend to react with protons to produce methane. In addition, the excited holes remained in the TiO_2 valence band after migration of excited electrons can also react with H_2O molecules on the catalyst surface to form active species $\cdot\text{OH}$ and H^+ ions. Eventually, CO_2 and water are photoreduced into CH_4 .

Compared with pure TiO_2 and solely doped TiO_2 , the photocatalytic activity of $\text{Pd}_{1.5}/\text{Zn}_5\text{-TiO}_2$ under UV-light irradiation is improved due to existence of both surface state energy level originated from the O-Zn-Cl species and surface state of PdO . This effectively facilitates the separation of photogenerated electrons and holes and thereby inhibits their recombination, resulting in more electrons and holes that can contribute to the photocatalytic reaction. Besides, as shown in table 3, the increased amount of bridging oxygen group (OH) may also contribute to the improved

photocatalytic activity. It can be seen that, doping Zn significantly increases the content of surface-bound OHs. Specifically, Pd_{1.5}/Zn₅-TiO₂ exhibits the highest content of surface-bound OHs. As discussed above, Pd_{1.5}/Zn₅-TiO₂ has the highest photocatalytic activity than that of pure TiO₂, Zn₅-TiO₂ and Pd_{1.5}-TiO₂.

References

- [1] Applied Catalysis B: Environmental 79 (2008) 208–215. Zn-doped TiO₂ nanoparticles with high photocatalytic activity synthesized by hydrogen–oxygen diffusion flame
- [2] Photocatalytic reduction of CO₂ to hydrocarbons using AgBr/TiO₂ nanocomposites under visible light 3.407
- [3] The Synergistic Effects of Two Co-catalysts on Zn₂GeO₄ on Photocatalytic Water Splitting
- [4] J.B. Zhong et al. / Journal of Hazardous Materials 168 (2009) 1632–1635
- [5] B. Zhu et al. / Catalysis Communications 9 (2008) 2323–2326
- [6] J.-J. Zou et al. / Journal of Molecular Catalysis A: Chemical 286 (2008) 63–69
- [7] A.-W. Xu, Y. Gao, H. Liu, J. Catal. 207 (2002) 151–157.
- [8] L. Jing, B. Xin, F. Yuan, L. Xue, B. Wang, H. Fu, J. Phys. Chem. B 110 (2006) 17860–17865.
- [9] Z. Wu et al. / Journal of Hazardous Materials 164 (2009) 542–548
- [10] Journal of Hazardous Materials 168 (2009) 1632–1635
- [11] Applied Catalysis B: Environmental 79 (2008) 208–215
- [19] G. Veser, A. Wright, R. Caretta, On the oxidation-reduction kinetic of palladium, Catal. Lett. 58 (1999) 199–206.
- [20] A.M. Venezia, L.F. Liotta, G. Deganello, Z. Schay, L. Guzzi, Characterization of pumice-supported Ag–Pd and Cu–Pd bimetallic catalysts by X-ray photoelectron spectroscopy and X-ray diffraction, J. Catal. 182 (1999) 449–455.
- (23) Kronik, L.; Shapira, Y. Surf. Sci. Rep. 1999, 37, 1-206.
- (24) Jing, L. Q.; Fu, H. G.; Wang, B. Q.; Wang, D. J.; Xin, B. F.; Li, S. D.; Sun, J. Z. Appl. Catal. B 2006, 62, 282-291
- (27) Xin, B. F.; Jing, L. Q.; Ren, Z. Y.; Wang, B. Q.; Fu, H. G. J. Phys. Chem. B

2005, 109, 2805-2809

(33) Jing, L. Q.; Sun, X. J.; Shang, J.; Cai, W. M.; Xu, Z. L.; Du, Y. G.; Fu, H. G. *Sol. Energy Mater. Sol. Cells* 2003, 79, 133-151.

(29) Gao, B.; Ma, Y.; Cao, Y.; Yang, W.; Yao, J. J. *Phys. Chem. B* 2006, 110, 14391.

[31] Z. Zhang, G. Mestl, H. Knozinger, W.M.H. Sachtler, Effects of calcination program and rehydration on palladium dispersion in zeolites NaY and 5A, *Appl. Catal. A* 89 (1992) 155–168.

[77] As described in the Experimental Section, the Pd-TiO₂ could not be calcinated in the air because of avoiding oxidation of Pd. However, most of the organic adsorbates should be removed by the washing treatment with water.

[30] L.Q. Jing, Z.L. Xu, X.J. Sun, W.M. Cai, *Appl. Surf. Sci.* 180 (2001) 308.

[32] J.G. Yu, H.G. Yu, B. Cheng, X.J. Zhao, J.C. Yu, W.K. Ho, *J. Phys. Chem. B*, 107 (2003) 13871.

[35] *Journal of Molecular Catalysis A: Chemical* 286 (2008) 63–69

(33) Mousty-Desbuquoit, C.; Riga, J.; Verbist, J. J. *J. Chem. Phys.* **1983**, 79, 26.

(34) Zhu, J.; Zheng, W.; He, B.; Zhang, J.; Anpo, M. *J. Mol. Catal. A* **2004**, 216, 35.

[40] L. Jing, B. Xin, F. Yuan, L. Xue, B. Wang, H. Fu, *J. Phys. Chem. B* 110(2006) 17860–17865.

(53) Jing, L. Q.; Xu, Z. L.; Sun, X. J.; Shang, J.; Cai, W. M. *Appl. Surf. Sci.* 2001, 180, 308-314

[50] Mudar Abou Asia, Chun Hea,b,*, *Catalysis Today*, 2011, 175, 256

[53] Zhengquan Li, Yujie Xiong, and Yi Xie*. *Inorganic Chemistry*, Vol. 42, No. 24, 2003, 8105

(43) Li, D.; Haneda, H.; Hishita, S.; Ohashi, N. *Chem. Mater.* **2005**, 17, 2596.

(44) Serpone, N.; Lawless, D.; Khairutdinov, R. *J. Phys. Chem.* **1995**, 99, 16655.

(45) Yu, J. C.; Ho, W.; Yu, J.; Hark, S. K.; Iu, K. *Langmuir* **2003**, 19, 3889.

(46) Saraf, L. V.; Patil, S. I.; Ogale, S. B.; Sainkar, S. R.; Kshirsager, S. T. *Int. J. Mod. Phys. B* **1998**, 12, 2635.

(60) *J. Phys. Chem. C*, Vol. 113, No. 49, 2009

[63] L.Q. Jing, X.J. Sun, J. Shang, W.M. Cai, Z.L. Xu, Y.G. Du, H.G. Fu, *Sol. Energ.*

Mater. Sol. Cells 79 (2003) 133.

introduction references

[3] S.C. Roy, O.K. Varghese, M. Paulose, C.A. Grimes, *Acs. Nano* 4 (2010) 1259.

[4] P.W. Pan, Y.W. Chen, *Catal. Commun.* 8 (2007) 1546.

[5] Q.H. Zhang, W.D. Han, Y.J. Hong, J.G. Yu, *Catal. Today* 148 (2009) 335.

[6] H.W. Slamet, E. Nasution, S. Purnama, J. Kosela, Gunlazuardi, *Catal. Commun.* 6 (2005) 313.

[7] Y. Bessekhoud, D. Robert, J.V. Weber, *J. Photochem. Photobiol. A: Chem.* 163 (2004) 569.

[8] P. Usubharatana, D. McMartin, A. Veawab, P. Tontiwachwuthikul, *Ind. Eng. Chem. Res.* 45 (2006) 2558.

Metal doped references

[5] Y. Li et al. / *Applied Catalysis B: Environmental* 100 (2010) 386–392

[6] I.H. Tseng, W.C. Chang, J.C.S. Wu, *Appl. Catal. B-Environ.* 37 (2002) 37–48.

[7] Y.H. Xu, D.H. Liang, M.L. Liu, D.Z. Liu, *Mater. Res. Bull.* 43 (2008) 3474–3482.

[8] O.K. Varghese, M. Paulose, T.J. LaTempa, C.A. Grimes, *Nano Lett.* 9 (2009) 731–737.

[9] O. Ishitani, C. Inoue, Y. Suzuki, T. Ibusuki, *J. Photochem. Photobiol. A-Chem.* 72 (1993) 269–271.

Nonmetals doped references

From Q. Zhang et al. / *Applied Catalysis A: General* 400 (2011) 195–202

[13] Y. Li, W.-N. Wang, Z. Zhan, M.-H. Woo, C.-Y. Wu, P. Biswas, *Appl. Catal. B: Environ.* 100 (2010) 386–392.

[18] N. Sasirekha, S.J.S. Basha, K. Shanthi, *Appl. Catal. B: Environ.* 62 (2006) 169–180.

[19] R. Dholam, N. Patel, *Int. J. Hydrogen Energy* 34 (2009) 5337–5346.

[20] M. Hamadani, A. Reisi-Vanani, A. Majedi, *Mater. Chem. Phys.* 116 (2009) 376–382.

[21] C. Wen, Y.J. Zhu, T. Kanbara, H.Z. Zhu, C.F. Xiao, *Desalination* 249 (2009) 621–625.

- [22] L. Zhou, J. Deng, Y. Zhao, W. Liu, L. An, F. Chen, *Mater. Chem. Phys.* 117 (2009) 522–527.
- [23] S. In, A. Orlov, R. Berg, F. Garcia, S. Pedrosa-Jimenez, M.S. Tikhov, D.S. Wright, R.M. Lambert, *J. Am. Chem. Soc.* 129 (2007) 13790–13791.
- [24] S.U.M. Khan, M. Al-Shahry, W.B. Ingler, *Science* 297 (2002) 2243–2245.
- [25] J.C. Yu, J.G. Yu, W.K. Ho, Z.T. Jiang, L.Z. Zhang, *Chem. Mater.* 14 (2002) 3808–3816.
- [26] G.S. Wu, J.L. Wen, J.P. Wang, D.F. Thomas, A.C. Chen, *Mater. Lett.* 64 (2010)
- Mechanism references**
- [27] I.H. Tseng, W.C. Chang, C.S. Wu, *Appl. Catal. B: Environ.* 37, 2002, 37.
- [28] H. Yamashita, Y. Fujii, Y. Ichihashi, S.G. Zhang, K. Ikeue, D.R. Park, K. Koyano, T. Tatsumi, M. Anpo, *Catal. Today* 45 (1998) 221.
- [29] S.S. Tan, L. Zou, E. Hu, *Catal. Today* 115 (2006) 269.
- [71] Surolia, P. K.; Tayade, R. J.; Jasra, R. V. *Ind. Eng. Chem. Res.* 2007, 46, 6196.
- [81] Cao, Y.; Yang, W.; Zhang, W.; Liu, G.; Yue, P. *New J. Chem.* 2004, 28, 218.